Multiple Surface Site Three-Dimensional Structure Determination of a Supported Molecular Catalyst

Ribal Jabbour, Marc Renom-Carrasco, Ka Wing Chan, Laura Völker, Pierrick Berruyer, Zhuoran Wang, Cory Widdifield, Moreno Lelli, David Gajan, Christophe Copéret, et al.

Multiple Surface Sites Three-Dimensional Structure Determination of a Supported Molecular Catalyst

Ribal Jabbour,[†] Marc Renom-Carrasco,[§] Ka Wing Chan,[‡] Laura Völker,[‡] Pierrick Berruyer,[o] Zhuoran Wang,[†] Cory M. Widdifield,[+] Moreno Lelli,[#] David Gajan,[†] Christophe Copéret,[‡] Chloé Thieuleux,[§*] Anne Lesage[†*]

† Université de Lyon, CNRS, ENS Lyon, Université Lyon 1, Centre de RMN de Lyon, UMR 5082, F-69100, 5 rue de la Doua, 69100 Villeurbanne, France

§ Université de Lyon, Institut de Chimie de Lyon, CP2M, UMR 5128 CNRS-CPE Lyon-UCBL, CPE Lyon, 43 Bvd du 11 Novembre 1918, 69100 Villeurbanne, France.

Magnetic Resonance Center (CERM), University of Florence, 50019 Sesto Fiorentino (FI), Italy

+ University of Regina, Department of Chemistry and Biochemistry, 3737 Wascana Parkway, Regina, SK, S4S 0A2 Canada

‡ ETH Zürich, Department of Chemistry and Applied Biosciences, Vladimir-Prelog-Weg 1-5/10, 8093 Zürich, Switzerland

o Institut des Sciences et Ingénierie Chimiques, Ecole Polytechnique Fédérale de Lausanne (EPFL), 1015 Lausanne, Switzerland

ABSTRACT: The structural characterization of supported molecular catalysts is challenging due to the low concentration of surface sites and the presence of several organic/organometallic surface groups resulting from the often complex surface chemistry associated with support functionalization. Here, we provide a complete atomic-scale description of all surface sites in a silica-supported iridium-N-heterocyclic carbene (Ir-NHC) catalytic material, at all stages of its synthesis. By combining a suitable isotope labelling strategy with the implementation of multi-nuclear dipolar recoupling DNP enhanced NMR experiments, the 3D structure of the Ir-NHC sites, as well as that of the synthesis intermediates were determined. As a significant fraction of parent surface fragments does not react during the multi-step synthesis, site-selective experiments were implemented to specifically probe proximities between the organometallic groups and the solid support. The NMR-derived structure of the iridium sites points to a well-defined conformation. By interpreting extended x-ray absorption fine structure (EXAFS) spectroscopy and chemical analysis data augmented by computational studies, the presence of two coordination geometries is demonstrated: Ir-NHC fragments coordinated by a 1,5-cyclooctadiene and one Cl ligand, as well as, more surprisingly, a fragment coordinated by two NHC and two Cl ligands. This study demonstrates a unique methodology to disclose individual surface structures in complex, multi-site environments, a long-standing challenge in the field of heterogeneous/supported catalysts, while revealing new, unexpected structural features of metallo-NHC supported substrates. It also highlights the potentially large diversity of surface sites present in functional materials prepared by surface chemistry, an essential knowledge to design materials with improved performances.

INTRODUCTION. Over the last forty years, tremendous efforts have been devoted towards the development of supported molecular catalysts as a route to deliver highly efficient catalytic systems that would combine the advantages of homogeneous catalysts with ease of separation and recyclability of heterogeneous catalysts, in addition to avoiding deactivation processes via dimerization or aggregation processes, frequently encountered in solution with molecular complexes.[1-3] However, despite these efforts, most supported systems have not met expectations in terms of catalytic performances,[4] thus limiting their interest for further development and applications in industrial settings. A major obstacle to this regard is the scarcity of reliable analytical approaches to gain a detailed atomic-scale description of the structure of surface species formed during the functionalization of the supports. A wide range of techniques are in principle available to characterize the surface of catalytic materials such as infrared (IR) spectroscopy, EXAFS (extended x-ray absorption fine structure) or XPS (x-ray photoelectron spectroscopy). However, these approaches alone cannot provide information on the local and spatial arrangement of the active sites. In addition, they usually fail to provide a correct description of surface species when those are structurally diverse, e.g. when the catalytically relevant sites adopt different coordination spheres or are surrounded by spectator groups such as residual reaction intermediates. Thus, decoding the full structural complexity of supported molecular catalysts remains an unmet challenge. This lack of a detailed molecular picture contrasts with the level of definition currently obtained for enzymes as an example of complex efficient catalysts and is currently a stumbling block to establish refined structure-activity relationships and thereby preventing rational catalysts development strategies.

In this context, solid-state NMR spectroscopy in combination with magic angle spinning (MAS) has become the method of choice to determine with atomic resolution the molecular structure of solids,

including supported catalysts in a variety of experimental conditions.[5] However, this spectroscopy suffers from inherently low sensitivity. This limitation is further exacerbated when the compound of interest is located on a surface, i.e. represents a tiny fraction of the sample, as is the case for immobilized catalysts. Hyperpolarization techniques have recently opened new analytical opportunities in catalysis.[6-8] In particular, dynamic nuclear polarization (DNP) has emerged as a powerful tool to examine dilute species at the surface of materials,[9-12] an approach called DNP SENS (DNP surface enhanced NMR spectroscopy). Recent applications in heterogeneous catalysis include the investigation of surface acidity in solid oxides,[13-16] the identification of reaction intermediates[17-18] or the elucidation of surface interactions,[19-20] to name but a few. DNP SENS has also been applied to characterize the structure of surface organometallic catalytic sites and probe their local environment.[21-28] Major steps forward have been recently achieved with the demonstration that the full three-dimensional (3D) structure of single-site metal complexes bound to amorphous silica or alumina surfaces could be probed by DNP SENS.[29-30] This was done by implementing multi-nuclear NMR experiments that provided a set of long-range structural constraints. Notably, internuclear proximities were experimentally measured between the solid support and the surface ligands that were used to determine the best-fit conformation of the organometallic fragment, as a single well-defined structure.

However, in many cases, the surface structure of heterogeneous supported catalysts is far more complex. In particular, the active sites of interest are often diluted among spectator species, i.e. among non-catalytically relevant units. This further impacts the sensitivity of the NMR experiments that could be implemented to target the detailed conformation of the catalytic complexes. In addition, in such cases, the multiple-site nature of the surface completely jeopardizes structural approaches based on the measurement of non-selective conformational constraints. This seriously limits the possibility to exploit the resulting models for reliable structure predictions. This is notably the case for catalysts prepared by incorporating complexes onto pre-functionalized solid supports, i.e. prepared upon a series of surface reactions. While the nature of anchoring sites and the grafting mechanism is nowadays well-understood on plain oxide supports like silica or alumina,[31-32] the chemistry of functionalized surfaces with organic ligands is far more challenging and complex, despite its apparent great resemblance with molecular chemistry. Thus, this is an area where the difficulty to predict the correct structure of the surface catalytic sites is the highest while surface characterization would be the most pertinent.

Here, we show that these limitations can be addressed by the implementation of a suitable isotope labelling strategy in combination with dipolar recoupling DNP enhanced NMR methods that *selectively* probe the proximity of the organometallic fragments to the surface without the influence of passive sites. We demonstrate the relevance and efficiency of this new approach with the determination of the 3D structure and distribution of conformer geometries for an iridium-N-heterocyclic carbene (Ir-NHC) supported catalyst containing multiple surface fragments all along its synthetic pathway, from the imidazolium precursor through the Ag-NHC intermediate. This material was chosen as it has shown unprecedented activities in alkene hydrogenation, much higher than molecular analogues, while the structure of the active sites remains elusive.[33-34] We find that extremely rich and chemically relevant insight can be obtained by this methodology. Notably, the DNP SENS-derived structure evidences a well-defined structure with two different coordination environments, one of them being counter-intuitive and not accessible in solution, that we model by density functional theory (DFT) calculations and EXAFS data. We also show that a large fraction of the surface sites in the final catalyst corresponds to unreacted imidazolium fragments. The incidence of these discoveries and of the unexpected structural complexity of the surface is discussed in terms of catalytic activity.

RESULTS AND DISCUSSION

Sample preparation and DNP formulation. The materials were prepared by co-hydrolysis and co-condensation of 19 equiv. of tetraethylorthosilicate (TEOS) with 1 equiv. of iodopropyltriethoxysilane in a sol-gel process using a templating route, in which the two precursors were first pre-hydrolyzed in acidic condition (pH = 1.5) and then co-condensed by the addition of NaF.[33] Sequencing the hydrolysis and condensation reactions ensures a good dispersion of the surfactant and silylated precursor in the mixture. Thus, in principle, this approach yields a regular distribution of the organic ligands inside the one-dimensional pore channels, [35-36] here of diameter ~6 nm and length ~1 μm, displaying a hexagonal 2D arrangement (Figure 1). However, it has been recently shown by Pruski and co-workers, [37-38] during the preparation of functional silica nanoparticles, that another stepwise approach with a templating route in basic conditions led to clusters of organic ligands due to the self-condensation of the precursors. Thus, we cannot definitively rule out the fact that some clusters of organic may be present on the surface.

Starting from a flexible iodopropyl fragment, a surface reaction yielded the imidazolium functionalities. The surface alkoxysilane/silanol groups were further transformed into trimethylsiloxane (TMS) in order to avoid side reactions with surface silanols (so-called surface passivation). This material is referred to as **Mat-Im**. An Ag-NHC material (**Mat-NHC-Ag**) was then prepared by the addition of a soluble silver source ($AgOC(CF_3)_3$). The Ir-NHC material (**Mat-NHC-Ir**) was finally obtained upon transmetallation with the $[IrCl(COD)]_2$ molecular complex. A detailed description of the synthesis is reported in the SI. Figure 1 describes schematically the synthetic pathway and shows the various surface species produced during the preparation of the catalytic material and investigated in this work. Beside the presence of NHC ligands, Ir is likely stabilized by other ligands, but the exact nature of the other ligands is not clear, although chlorine ligands are expected to be present (vide infra). Six isotopically-labelled materials were prepared, with ^{15}N labels at the first (N1) or second position (N2) of the imidazolium ring: **Mat(1)-Im**, **Mat(1)-NHC-Ag**, **Mat(1)-NHC-Ir**, **Mat(2)-Im**, **Mat(2)-NHC-Ag**, **Mat(2)-NHC-Ir**. In all of them, the carbene (at position C6) was ^{13}C-labeled. This was intended to provide structural information on the orientation of the imidazole ring. The CH_3 groups of the surface trimethylsiloxyl and of the mesityl moieties were deuterated in order to ensure long DNP polarization build-up times and high DNP enhancement factors.[39]

All the NMR spectra were recorded under DNP conditions at a magnetic field of 9.4 T (see the Experimental Section for details). The samples were prepared by impregnating the dry powder with a polarizing solution of 1,1,2,2-tetrachloroethane (TCE) containing TEKPOL[40] radical at a concentration of 16 mM. Proton enhancement factors of between 30 and 100 were typically measured at ~110 K. The relatively large size of the TEKPOL molecules ensures that they will not thoroughly enter the longitudinal pores of the silica matrix[41] and that the surface sites will be polarized by spin diffusion through the solvent inside the pore. DNP data measured on model

mesoporous silica supports prepared with the same sol-gel process yielded a contribution factor of 0.8, indicating that TEKPOL only penetrates in the first ~10% of the pore volume (Figure S23). This is a key experimental aspect, implying that relatively long nuclear transverse coherence lifetimes (T_2') will be preserved for surface species not in contact with the radical. This will enable the implementation of efficient solvent suppression schemes and, more importantly of dipolar recoupling experiments.

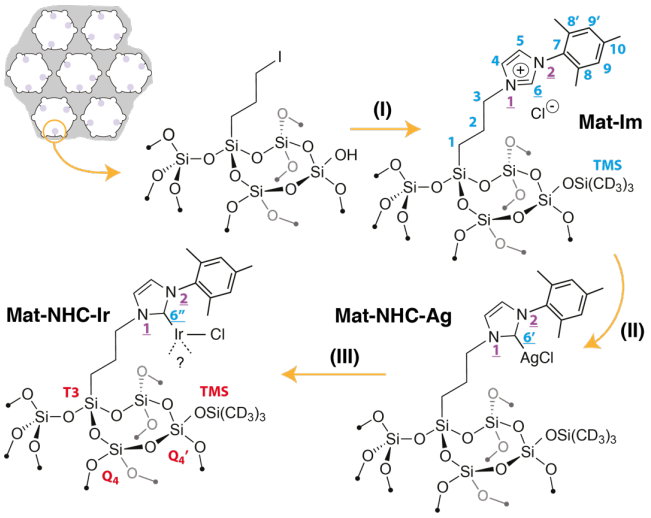

Figure 1. Schematic representation of the reaction pathway that leads to the preparation of the **Mat-NHC-Ir** material. The numbers used to identify the various carbon, nitrogen and silicon atoms is indicated in blue, purple and red respectively. The positions where ^{15}N and ^{13}C labels were introduced are underlined. **(I)** Post-reactions to give an imidazolium-containing material with deuterated mesityl rings and TMS groups. **(II)** $AgOC(CF_3)_3$ in CH_3CN at 25 °C in the absence of light. **(III)** $[Ir(COD)Cl]_2$ in CH_3CN at 60 °C in the absence of light. Details are given in the SI.

Resonance assignment and evidence for multiple surface species. The ^1H, ^{13}C, ^{15}N and ^{29}Si NMR resonances of the imidazolium precursor and of the silver and iridium complexes were assigned from one-dimensional (1D) DNP-enhanced cross-polarization (CP) and two-dimensional (2D) heteronuclear correlation (HETCOR) NMR spectra. Figure 2 shows the ^{13}C and ^{15}N CPMAS spectra of **Mat(1)-Im**, **Mat(1)-NHC-Ag** and **Mat(1)-NHC-Ir**. The 2D ^1H-^{13}C HETCOR spectra are reported in Figure S9, while Figure S10 displays ^{29}Si NMR data. The 2D ^1H-^{13}C HETCOR spectra show all the expected correlations. In particular, the silver and iridium carbenes (C6' and C6") receive polarization during CP from both aliphatic protons of the propyl chain and from aromatic protons of the NHC ring. Figure 2(d) shows the silicon-29 CPMAS spectrum of **Mat(1)-Im**. The ^{29}Si NMR spectra of the other materials were identical (Figure S11). They all display four resonances that are assigned to the TMS groups at around 0 ppm, to the T_3 sites at -80 ppm and to the Q_4 and Q_4' sites at respectively -120 and -114 ppm. The Q_4' sites correspond to silicon atoms of the matrix directly bound to the TMS groups. The Q_4 and Q_4' signals were deconvoluted for the analysis of the REDOR curves (*vide infra*). Correlations are observed with some aliphatic and aromatic protons of the organic fragment and possibly with the TCE proton resonance expected at around 6 ppm, as illustrated in Figure S10 for **Mat(1)-Im**. The NMR chemical shifts are reported in Table S6.

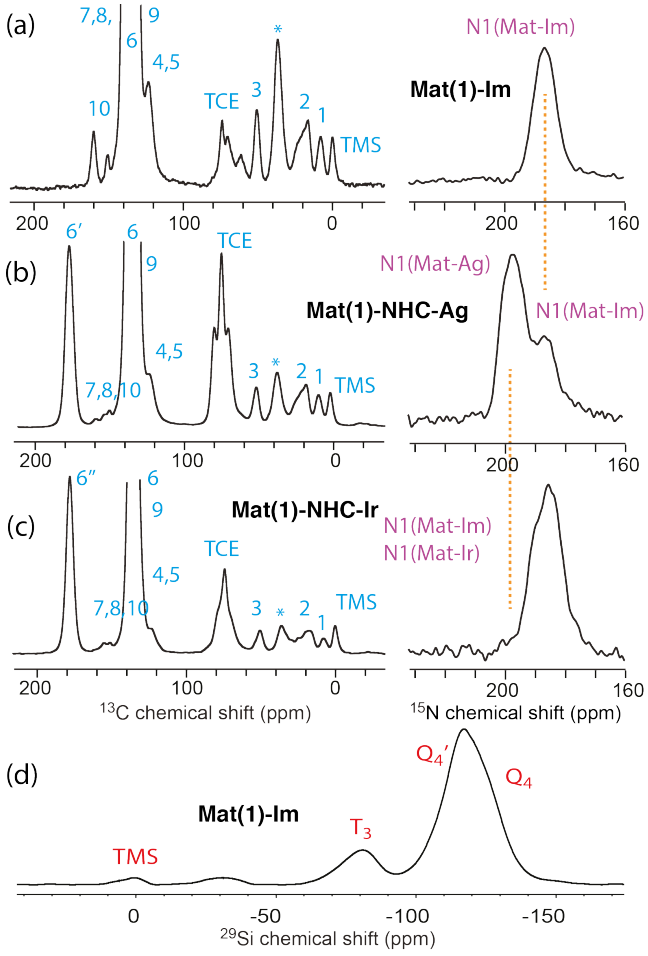

Figure 2. One-dimensional DNP enhanced CPMAS ^{13}C and ^{15}N NMR spectra of (a) **Mat(1)-Im**, (b) **Mat(1)-NHC-Ag** and (c) **Mat(1)-NHC-Ir**. The asterisk * corresponds to the spinning side -band of the C6 resonance. The ^{13}C spectra were recorded with solvent suppression. (d) One-dimensional ^{29}Si CPMAS spectrum of **Mat(1)-Im**. T_3 sites refer to silicon sites with three Si-O-Si bonds and one Si-C bond and Q_4 sites to silicon sites with four Si-O-Si bonds. Silicon Q_4 sites linked to a TMS group were labeled Q_4' according to the scheme of Figure 1. The Q_4' resonance was assigned in reference 35 from a ^{29}Si-^{29}Si INADEQUATE experiment. Experimental details are reported in the SI, as well as two-dimensional ^1H-^{13}C and ^1H-^{29}Si correlation spectra.

The analysis of the NMR spectra allowed not only the identification of the resonances of each surface species, but also enabled one to monitor the chemical reactions carried out on the surface functionalities. The resonance of the ^{13}C-labelled C6 carbon in the NMR spectrum of **Mat(1)-Im** can be readily identified from its huge intensity at 133.7 ppm in Figure 2(a). The conversion of the imidazolium precursor to the silver complex is evidenced by the appearance of a new resonance at 178.6 ppm corresponding to the C6' carbon of the silver complex in Figure 2(b). A resonance at around the same chemical shift C6" is observed in the ^{13}C spectrum of **Mat(1)-NHC-Ir** (Figure 2(c)). The C6 signal that corresponds to the imidazolium unit is however still present in spectrum of Figure 2(b), which indicates that the conversion from the imidazolium fragment to the intermediate silver complex is not complete, and that a significant amount of the surface imidazolium fragment remains on the surface. This is corroborated by the ^{15}N NMR spectrum of **Mat(1)-Ag-NHC** that displays two resonances. Conversely, a single broad peak

is observed on the ^{15}N NMR spectrum of **Mat(1)-Ir-NHC**, which reveals that the transmetallation step is quantitative and the NHC-Ag surface species are no longer present in the iridium material. In summary, the **Mat(1)-NHC-Ag** and **Mat(1)-NHC-Ir** materials are composed of a mixture of surface species, namely the imidazolium precursor in addition to the Ag-NHC or the Ir-NHC surface complexes respectively. Similar observations were made with the materials having a ^{15}N-label at position 2 of the imidazolium NHC ring (Figure S12). We note that the ^{13}C and the ^{15}N NMR spectra of Figure 2 were recorded using a cross-polarization step from protons, and therefore are not quantitative. In order to obtain quantitative estimates on the reaction yields, carbon-13 single pulse experiments were recorded on **Mat(1)-NHC-Ag**, **Mat(1)-NHC-Ir**, **Mat(2)-NHC-Ag** and **Mat(1)-NHC-Ir** (Figure S13). If the recycle delay is long enough to allow all carbon-13 spins to go back to equilibrium, the ratio of peak integrals for the C6 resonance (including the spinning sidebands) provides the conversion yield from the imidazolium precursor to the silver intermediate, and from this latter to the Ir complex, in the fraction of surface species observed by DNP SENS. Similar experiments were conducted on **Mat(2)-NHC-Ag** and **Mat(2)-NHC-Ir** materials. Estimation of the reaction yields, as seen from NMR spectroscopy, are summarized in Figure S14. Overall, between 25 and 30% of the imidazolium functionalities are converted to silver complexes, and between 15 and 20% from parent imidazolium functionalities are *in-fine* converted in iridium complexes. These values suggest that, while the transmetallation process is complete, a fraction of the Ag complexes is converted back to imidazolium moieties. Here, we note that these yields are inaccessible by conventional methods such as chemical titration, as insoluble silver salts are released that stick on the surface of the solid support after transmetallation. NMR in combination with isotopic labelling is therefore the only way to obtain of a rough estimation of the surface reaction yields.

The presence of two distinct surface species in **Mat-NHC-Ag** and **Mat-NHC-Ir**, namely the imidazolium unit and the metallic complexes, drastically complicates the structural characterization of the surface sites in these materials. This difficulty is further amplified by the fact that, except for the C6 signal, all the other carbon resonances of the imidazolium precursor, of the silver and of the iridium complexes have similar chemical shifts. Similarly, the ^{15}N resonances of the imidazolium ligand and of the Ag/Ir-NHC complexes are at the same position or are extremely close, and thus cannot be exploited as species-specific probe nuclei. As described in the next section, several advanced NMR strategies were developed, including the implementation of frequency-selective experiments, in order to determine the ensemble of structures of each surface functionality.

Distance constraint measurements. As the nitrogen atoms, either N1 or N2, and the carbon C6 are respectively ^{15}N- or ^{13}C-labelled, a suite of ^{13}C-{^{15}N1}, ^{13}C-{^{15}N2}, ^{29}Si-{^{15}N1}, ^{29}Si-{^{15}N2} and ^{29}Si-{^{13}C6} Rotational Echo Double Resonance (REDOR) experiments[42] were implemented to probe long-range structural distances. REDOR experiments rely on the reintroduction of the MAS-averaged heteronuclear dipolar coupling between two (assumed) isolated spins X and Y. This is achieved by applying a series of rotor-synchronized π-pulses on the Y channel (Figure S15). The transverse magnetization of the X spin undergoes a dipolar dephasing that leads to an attenuation of the signal intensity S with increasing length of the echo periods. A control experiment is recorded, in the absence of π-pulses on the Y channel, in which the intensity S_0 accounts only for T_2' losses. The ratio S/S_0 as a function of the echo time provides a dephasing from which the dipolar coupling, and thus the internuclear distance can be extracted.

Conventional REDOR experiments implemented on **Mat(1)-Im** and **Mat(2)-Im** yielded a set of 10 dipolar dephasing curves as shown in Figure 3. We note that some proximities could not be probed because the signal-to-noise ratio was insufficient, as was the case for the Si_{TMS}-N2 or C2-N2 proximities. As mentioned previously, the C6 carbene signal has a different chemical shift in the imidazolium precursor and in the organometallic complexes. In order to selectively measure structural constraints in these latter fragments, Frequency-Selective (FS) REDOR experiments[43] were implemented where a selective pulse was applied on the C6 resonance of the silver or iridium complex. This led to the measurements of 3 non-ambiguous spatial proximities between the C6 carbon and silicon sites in **Mat(1)-NHC-Ag** and **Mat(1)-NHC-Ir**. As the ^{15}N resonances of the imidazolium unit and those of the organometallic complexes are extremely close, if not the same, ^{29}Si-{^{15}N} FS REDOR could not be meaningfully carried out to measure proximities between the silica matrix and the ^{15}N probe nuclei of the organometallic functionalities. Nevertheless, conventional (i.e. non-selective) ^{29}Si-{^{15}N} REDOR experiments were recorded on **Mat(1)-NHC-Ag**, **Mat(2)-NHC-Ag**, **Mat(1)-NHC-Ir** and **Mat(2)-NHC-Ir** and analyzed from the knowledge of the dipolar dephasing curves measured on **Mat(1)-Im** and **Mat(2)-Im**. Indeed, in these cases, the dipolar dephasing curves are a sum of two decays, corresponding to ^{29}Si sites close to the imidazolium precursor as well as to sites near the silver or the iridium complex. The weight of each fraction in this sum corresponds to the relative quantity of species present at the surface of the silica matrix, as determined above. The ^{29}Si-{^{15}N} REDOR curves measured on **Mat(1)-Im**, **Mat(1)-NHC-Ag** and **Mat(1)-NHC-Ir** were compared (Figure S19 and S20). They exhibit a fairly similar dephasing for the imidazolium precursor material on the one hand and the silver- or the iridium-NHC material on the other hand. Therefore, the non-selective ^{29}Si-{^{15}N} REDOR curves recorded on **Mat-NHC-Ag** and **Mat-NHC-Ir** were used in the structure calculation protocol of the Ag-NHC and Ir-NHC functionalities. Thus, for these latter, 7 long-range constraints were taken into account. Here we note that the signal intensity of silicon Q'_4 sites was obtained by deconvoluting the main resonance at around -120 ppm (Figure S11). The REDOR curves for the Q_4 sites were not considered in the structure calculation.

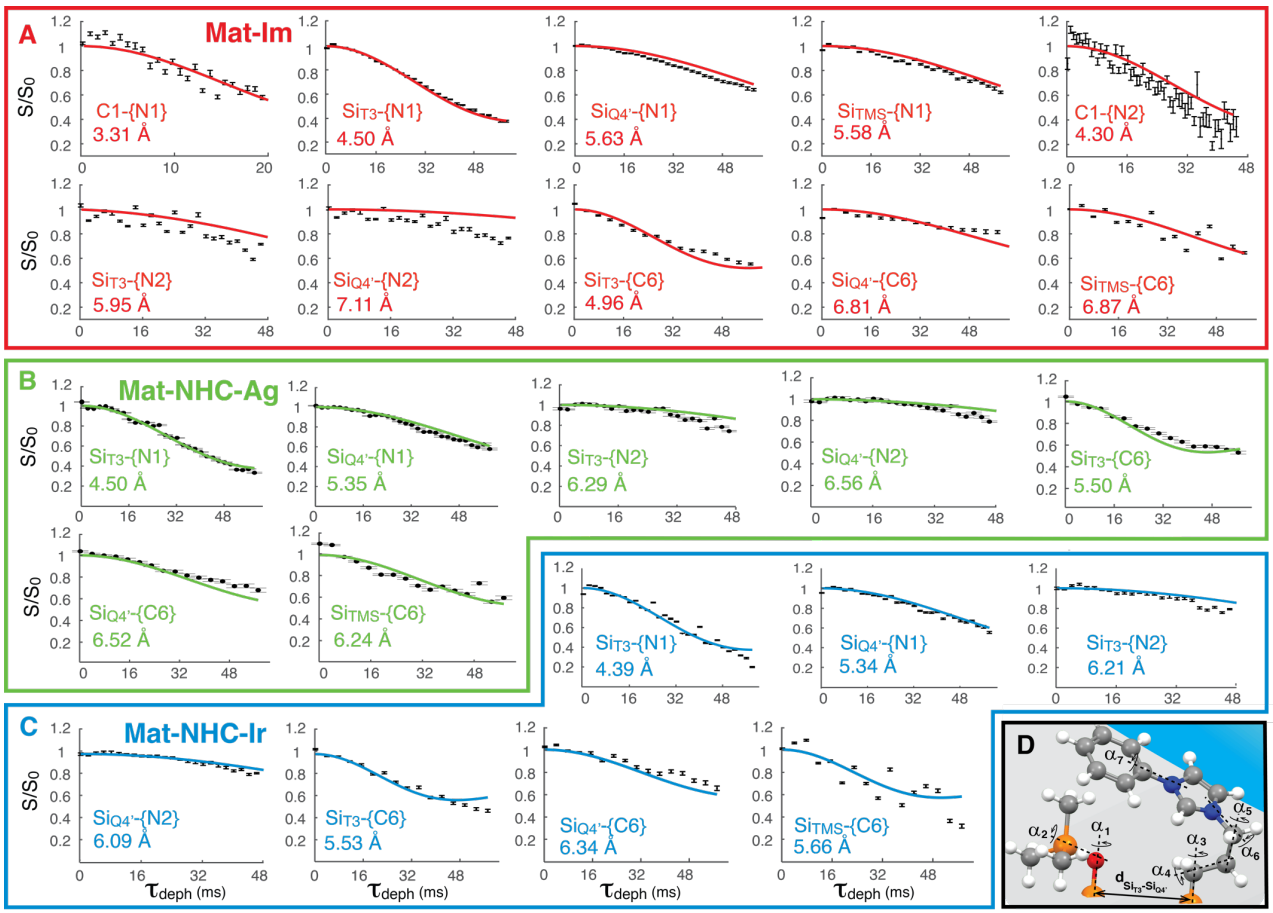

Figure 3. Experimental dipolar dephasing REDOR curves measured on the imidazolium precursor ((A), rex box), the silver ((B), green box) and iridium materials ((C) blue box). The Si-{C6} curves reported here were measured on **Mat(1)-Im**, **Mat(1)-NHC-Ag** and **Mat(1)-NHC-Ir**. The solid red, green and blue lines are REDOR curves calculated from internuclear distances directly measured on the structures in best agreement with the experimental data (i.e. they do not result from the fit of the dephasing curves). The internuclear distances measured in these structures are reported for each curve.

Protocol for structure determination. The three-dimensional structure of the imidazolium precursor, the silver-based intermediate complex and the iridium-based catalyst were determined by applying the protocol introduced for the Pt-NHC complex by Berruyer *et al*,[29] and adapted to the specificities of the systems investigated here. The overall procedure is detailed in the SI (Figure S16). As the molecular structure of the surface species is of small size and in addition, anchored to a solid support, the number of conformational degrees of freedom is limited. Seven rotation angles were considered as depicted in Figure 3(D) and, on the basis of previously developed models of silica surfaces,[44] three representative values of 4.50 Å, 5.59 Å and 5.83 Å were investigated for the distance between the Si_{T3} and $Si_{Q4'}$ atoms. The rotation around α_2 within the TMS group was set to an arbitrary value, while the rotation around α_7 was set to 120°, i.e. the value found from the X-ray data set on the homogeneous analog of the Ir-NHC catalyst.[33] The conformational space was sampled by varying α_1, α_3, α_4, α_5, and α_6 angles independently by increments of 15° so as to generate a large pool of candidate structures. For each candidate structure, REDOR curves were calculated using the analytical expression for S/S_0 (as reported in the SI). The deviation between the predicted data for a given structure and the experimental data was then computed by calculating the sum of squared residuals for all the REDOR curves. The structure in best agreement with the experimental data is defined as the one with the lowest deviation value, R. As mentioned above, for the **Mat-Im** material, a set of 10 REDOR curves were jointly analyzed, while only 7 curves were considered for the **Mat-NHC-Ag** and **Mat-NHC-Ir** materials. As detailed in the SI, cross validation was applied using random subsampling of experimental data (i.e. a number of points was randomly removed from the experimental REDOR curve) to determine the ensemble of structures. In each case, the cross-validation process was repeated 200 times and the best fit structure was stored. The ensemble of best fit structures yields the distribution of possible structures at the surface. Before structure calculation, the scaling factor of each REDOR curve was determined from REDOR data corresponding to internuclear distances that are fixed in the molecular geometry (Figure S17 and S18).

Three-dimensional structures derived from the DNP SENS data. The single 3D structures in best agreement with the experimental data are shown in Figure S21 for the imidazolium precursor, the Ag-NHC and Ir-NHC complexes. The corresponding REDOR curves, calculated from these best fit structures using the analytical expression of S/S_0, are superimposed on the experimental REDOR data of Figure 3. While the imidazolium functionality appears to be folded towards the surface, with internuclear

distances to the silicon T3 sites that are analogous to those measured on the Pt-NHC (Table S7), the Ag- and Ir-NHC moieties display rather extended conformations. In none of the structures is a close proximity between the C6 (or C6' and C6") carbon and the oxygen of the TMS group detected. Figure 4 shows the ensemble of best fit structures obtained from the cross-validation process for the three types of surface species. For the imidazolium precursor, two distinct and relatively symmetric sets of ensembles were found where the α_1 and α_3 angles differ by around 180°. Within these two sets of ensembles, 7 (for the left set) and 8 (for the right set) different structures were obtained, yielding RMSD values (calculated on the carbons of the tether and on the two nitrogen atoms) within each ensemble of respectively 2.17 and 0.84 Å. A similar process was applied to validate the structure of the silver and iridium complexes, and to access the ensemble of conformations. For the silver complex, a total of 11 different structures were found, with an RMSD of 3.49 Å. Similarly, an ensemble of 14 structures were found for the iridium complex, with an RMSD of 0.89 Å. The structures of Figure S21 and Figure 4 were calculated with a distance of 5.59 Å between the $Si_{Q4'}$ and the Si_{T3} sites. For the imidazolium precursor, calculations were also done for two other distances of 4.50 and 5.83 Å derived from the amorphous silica surface model by Ugliengo *et al.*[44] In these two cases, the best fit structure was the same as that determined for a 5.59 Å distance. Here we note that these ensembles of structures represent a set of static models that are in agreement with the experimental data. As such, they do not provide clues for molecular dynamics at ambient temperature.

While the ensemble of structures obtained for the surface silver complex is relatively broad with a RMSD value of 3.49 Å, a much more limited set of conformations was derived from the calculation protocol for the Ir-NHC fragment. Although only 7 structural constraints were used in the calculation versus 10 for the surface imidazolium fragment, a well-defined structure with a RMSD of 0.89 Å emerged for the surface iridium complex. However, unlike the initial expectations, the structure clearly shows that the Ir-NHC fragment is not folded back onto the surface but rather points outward into the porous cavity. In particular, the distance between the iridium and the oxygen atom that resides between the $Si_{Q4'}$ and Si_{TMS} is 7.6 Å.

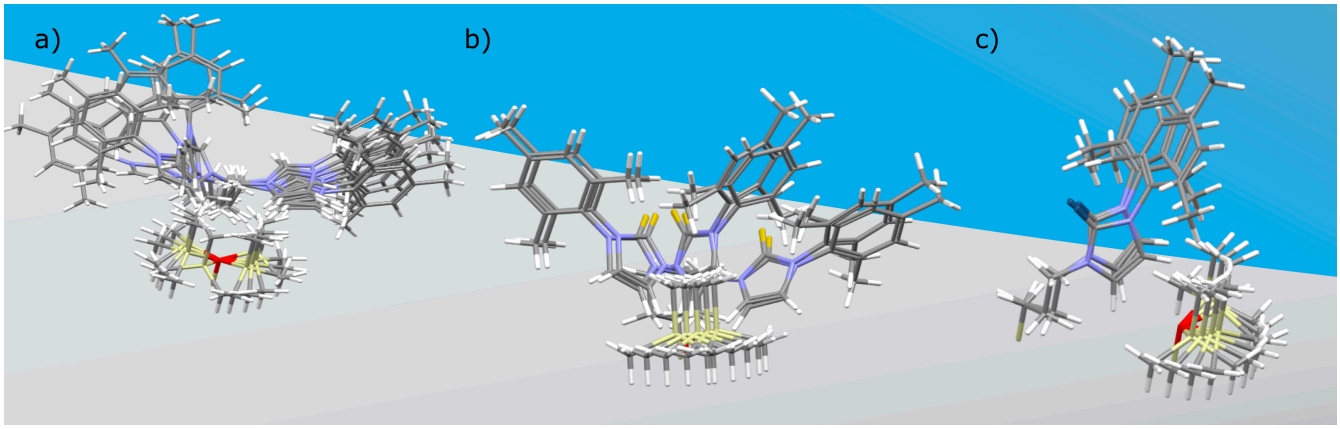

Figure 4. Ensemble of conformers obtained for the three surface species: the imidazolium precursor (a), the Ag-NHC intermediate complex (b), and the Ir-NHC catalytic complex (c). The structures were superimposed by aligning the Si_{T3}, $Si_{Q4'}$ and O attached to the $Si_{Q4'}$. These ensembles are calculated from the NMR REDOR curves. In b) and c) an Ag and Ir atoms have been added to highlight the orientation of the metal center (note however that the structures determined at this stage do not represent the final models).

Thus, in the 3D structure derived from the DNP SENS data, the iridium metal center is clearly not coordinated by this surface oxygen, nor by any other surface oxygen atoms. We note here that the main difference in the set of constraints used to calculate the structure of the silver and iridium functionalities lies in the Si_{TMS}-{C6} dephasing curve. Figure S24 compares the ^{29}Si-{^{13}C6} experimental data measured on the three materials.

The structure calculation protocol used here was adapted from reference 35 where it was benchmarked on a model Pt fragment that was selected as a representative catalytic surface site. In this proof-of-concept study by Berruyer et al, the possible presence of multiple surface species has been overlooked. Because we have now introduced a ^{13}C label at the C6 position of the imidazolium/NHC ring, large amounts of unreacted surface organic fragments became clearly visible. The presence of these "spectator species" was considered here in structure determination, via the implementation of site-selective distance measurements. In addition, this more elaborate labelling strategy allowed one to use of a larger variety of structural constraints to calculate structures along the chain of surface chemistry reactions.

Extended X-ray Absorption Fine Structure (EXAFS) of Mat-NHC-Ir. In order to obtain insight into the (average) coordination environment of iridium in the Ir-NHC material, EXAFS analysis was performed. Figure S25 shows the EXAFS data measured on the **Mat-NHC-Ir** material and Table 1 indicates the number and nature of atoms surrounding the iridium center as a result of the fitting procedure. In this first fit, one Cl atom was postulated (model A). The data in Table 1 suggest that the number of carbon neighbors around the Ir center is 3 ± 1 at 2.11 ± 0.02 Å along with the Cl atom at 2.39 ± 0.02 Å. However, adding oxygen atoms in the coordination sphere of the iridium center does not improve the fit, indicating that in these materials with high ligand density, there is no (or little) interaction (binding) of Ir with the oxygen surface functionalities. However, the EXAFS data and the NMR-derived structure suggest a different number of carbon ligands: 3 carbon atoms nearby the iridium for EXAFS vs. only one carbon for NMR-derived structure (see below).

Table 1. EXAFS fit parameters for the Ir L_3-edge spectrum of **Mat(1)-NHC-Ir.**

Model	neighbor	N[a]	σ^2 (Å^2)[b]	R (Å)[c]
A	C	3 (1)	0.006 (2)	2.11 (2)
	Cl	1*	0.007 (2)	2.39 (2)
B	C	2.3 (7)	0.006 (3)	2.10 (2)
	Cl	1.5*	0.010 (2)	2.38 (2)

[a]Number of specified neighbors. [b]Debye-Waller factor. [c]Distance between Ir metal center to the specified neighbors. *Fixed parameter in the fit.

Iridium coordination sphere. To resolve this apparent discrepancy between the DNP SENS-derived structural model of the Ir-NHC complex and the EXAFS data, two coordination environments were considered: an Ir-NHC fragment coordinated by a 1,5-cyclooctadiene (COD) ligand and a bis-NHC Ir complex. This latter environment is postulated given the relatively high density of imidazolium units in the starting material and the possibility for the Iridium center to coordinate two NHC units.

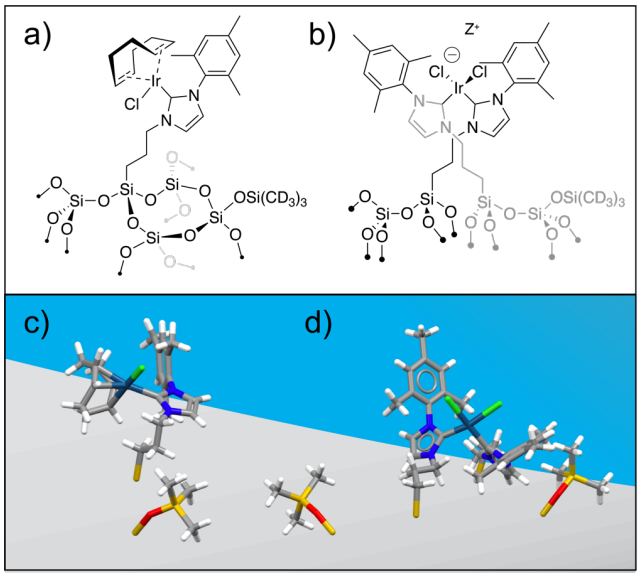

Figure 5: (a) and (b) Chemical structures of the [Ir(NHC)(COD)Cl] and the [Ir(NHC)$_2$Cl$_2^-$] ligands, respectively, on the silica surface and within **Mat-NHC-Ir**. (c) and (d) Three-dimensional structure of the two types of complexes, after DFT geometry optimization, starting from the experimentally determined best fit structure of the Ir-NHC complex.

As detailed in the synthesis protocol, the iridium center is introduced *via* a [Ir(COD)Cl]$_2$ molecular complex. We therefore first postulated that the COD ligand might still be present around the surface Ir metal centers, stabilizing the whole organometallic complex (Figure 5(a)). In order to validate this hypothesis, **Mat-NHC-Ir** was suspended in dry toluene and put under 3 bars of H_2 and the amount of cyclooctane released after hydrogenation was quantified to estimate the number of COD coordinated to the Ir centers in the material. The data show that ca. 45 % of the Ir sites contain a residual COD ligand (details in the SI). We note here that the ^{13}C NMR resonances of the COD ligand (expected at around 30 ppm for the methylene signals, and at around 50 ppm and 80 ppm for the sp^2 carbon atoms) could not be unambiguously observed in the DNP SENS ^{13}C spectra of Figure 2c, as they are masked by the huge solvent resonance and by the aliphatic resonances of the propyl tether of the organic ligand. We note however that in the 2D ^{1}H-^{13}C HETCOR spectrum of the **Mat-NHC-Ir** material reported in Figure S9(c), weak cross-peaks, e.g. at around (ω_1,ω_2) = (78 ppm, 2 ppm) are observed that could be consistent with the presence of COD. Similarly, ^{13}C-{^{15}N} REDOR spectra recorded after recoupling times of a few ms and where the solvent signal is efficiently suppressed by fast transverse dephasing, reveal the presence of a weak resonance at ~78 ppm, which might correspond to one of the two CH resonance. To confirm our hypothesis, room temperature ultra-fast MAS ^{1}H 1D and 2D double-quantum single-quantum NMR experiments were acquired on the **Mat(1)-NHC-Ir** (Figure S26 and S27). They reveal new resonances that agree with the presence of COD moieties. We note that the presence of remaining COD ligands explains why the number of coordinating carbons obtained from the fit of the EXAFS data is higher than our initial expectation.

The chemical analysis mentioned above shows that roughly half of the Ir sites are coordinated by a COD ligand. A second coordination structure was therefore investigated, where the Ir metal center is surrounded by two NHC ligands (Figure 5(b)). Such structures are well-known in homogeneous catalysis,[45] but have never been spectroscopically confirmed so far for supported complexes as the isolation of the surface sites usually prevent the formation of such edifices. Figure 6(a) shows the 2D ^{13}C INADEQUATE NMR spectrum recorded on **Mat(1)-Ir-NHC** under DNP conditions. A clear DQ-SQ correlation is observed at (ω_1,ω_2) = (356 ppm, 178 ppm) that indicates the presence of C6"-C6" through-bond coupling for some of the surface Ir-NHC species. A carbon-carbon *J* coupling of about 25 ± 2 Hz is estimated from the evolution of the C6" signal intensity as a function of the reconversion period in 1D INADEQUATE NMR spectra (Figure 6(b)). These experiments demonstrate the presence of supported bis-NHC iridium complexes.

Density functional theory (DFT) geometry optimizations, starting from the experimentally determined best fit structure of the Ir-NHC complex were performed for both types of Ir coordination. One and two chlorine atoms were added in the local iridium coordination sphere for the NHC(COD) and bis-NHC complexes, respectively. Extracts of the optimized structures are shown in Figure 5(c) and (d), with full coordinates being provided in the SI. The bis-NHC iridium complex is anionic, with counterions being possibly silver cations remaining from the multi-step synthesis. The C6 chemical shifts calculated on the full DFT-optimized 3D structures (Table S8) as well as on model Ir complexes (Table S9), are in reasonable agreement with the experimentally observed shift at around 178 ppm. These calculations provide additional support for the coordination sphere proposed here for the two supported complexes.

We note that a mixture of these two structures in a roughly 0.45 (for the Ir-NHC complex with a COD ligand) to 0.55 (for the Ir-bis-NHC species) ratio (according to the COD titration mentioned preaceviously and reported in the SI) would lead to an average number of carbon atoms around the metal center of 3.35. This number agrees relatively well with the EXAFS data that were again fitted using 1.5 Cl atom (model B), and provide a number of 2.3±0.7 carbons. Importantly, the orientation of the C6-Ir bond points away from the silica surface, as in the NMR derived-structure (Figure 4(c)), and is compatible with the coordination by a COD ligand or by two NHC fragments. Finally, we note that the ^{29}Si-{C6} REDOR curves calculated from internuclear distances measured on a 1:1 ratio of the two optimized structures are in good agreement with the site-selective experimental ones as show in Figure S30.

Implications for the catalytic activity. Our study reveals a large diversity of structures onto the catalytic surface. This surface is occupied by a significant fraction of leftover organic fragments (around 70%), a surprising result as the formation of the Ag-NHC complex from the imidazolium units using molecular homologues in solution is quantitative. This observation can be explained by the fact that the imidazolium surface fragment displays a possibly broad range of structures that are folded towards the surface, which may prevent its accessibility and reactivity, leading to a low metalation rate. This finding illustrates that major reactivity differences can be observed between solution and surface chemistries.

Our study also demonstrates the presence of two types of Ir-NHC sites in a roughly similar ratio, among which an Ir bis-NHC complex that was completely unexpected and observed here for the first time in a supported catalyst. The two types of Ir-NHC complexes appear as well-defined structures, stabilized by COD and/or chloride ligands.

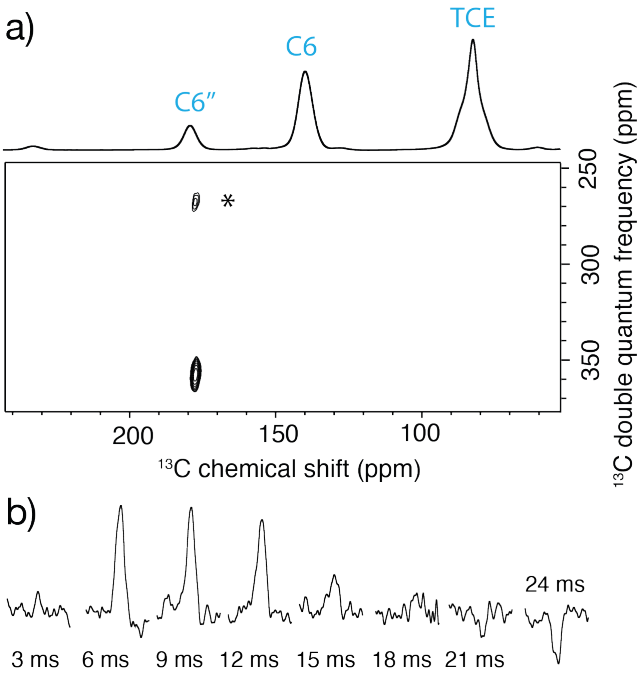

Figure 6. (a) Two-dimensional DNP enhanced ^{13}C refocused INADEQUATE spectrum of **Mat(1)-NHC-Ir**. Experimental details are given in the legend of Figure S28. The asterisk indicates a spinning sideband. The 1D carbon-13 CPMAS spectrum is shown above the 2D plot. (b) Modulation of the C6" signal intensity recorded in 1D INADEQUATE spectra as a function of the second delay τ_2. The first delay τ_1 was set to 8 ms.

A structure where the Ir center was coordinated by surface oxygen atoms was previously proposed by us in Ir-NHC materials prepared with a lower concentration of surface imidazolium fragments (using a TEOS:organosilane ratio of 30[33] versus 19 here). This lower density leads to more isolated sites and likely prevents the coordination of two NHC ligands on one Ir center. Additionally, only traces of COD were observed in this material. Here, the high density of surface NHC groups explains the residual presence of the COD ligand on the Ir mono-NHC sites as well as the formation of Ir bis-NHC complexes. Thus, various initial concentrations of ligands on functionalized surfaces may lead not only to different structures of organometallic complexes but also to the co-existence of several active sites. This is again a key observation, showing that tiny differences in the preparation of functional solids can lead to dramatic differences in the nature of the surface sites. However, it is worth pointing out that the catalytic activity per iridium atom of the two Ir-NHC materials prepared with two different density of sites is exactly the same, both types of materials being highly active and productive in alkene hydrogenation.

In order to compare the activity of the two materials, the following catalytic tests were performed: hydrogenation of trans-stilbene was carried out using ca. 0.1 mol% of Ir under 3 bars of H_2 at 40°C during 18 hours. The results show very similar TOF (turn over frequency) and TON (turn over number) for both solids (TOF (TON): 47 h^{-1} (800) vs 42 h^{-1} (755), for the present material and for the previously prepared one, respectively), pointing out that the catalytic activity per iridium atom is similar and that both materials are equally highly active and productive in alkene hydrogenation. These results also suggest that both Ir-mono-NHC and Ir-bis-NHC sites are similarly active in catalysis. However, developing a solid containing exclusively Ir-bis-NHC surface sites, for example using an even higher site density, would be essential to fully understand and quantify the intrinsic catalytic performance of mono- and bis-NHC species.

Although the catalytic performance is unchanged, the ability to prepare mono- or bis-NHC iridium surface sites depending on the site density is an important discovery that paves the way to the development of single-site supported catalysts containing one or the other complex.

CONCLUSION

The atomic-scale structure of all the surface sites present in a catalytically active mesostructured silica material containing Iridium N-heterocyclic carbene complexes was determined by DNP enhanced multi-nuclear and multi-dimensional NMR spectroscopy. The structures of the synthesis intermediates that precede the formation of the Ir complex along the synthesis pathway were also investigated. We showed that unreacted organic precursors (surface imidazolium fragments) represent a significant fraction of the surface species in the iridium- and silver-based materials (in contrast to what is observed in solution using molecular homologues). The presence of several surface sites substantially complicates the structural investigation. To overcome this challenge, dedicated site-selective NMR strategies were implemented. The structure determination protocol converged to an atomic-scale conformation where the Ir center is pointing away from the silica surface, excluding the coordination by surface oxygen atoms. By interpreting jointly EXAFS and chemical analysis data, two different Ir coordination spheres were proposed and experimentally confirmed: an Ir-NHC fragment coordinated by a 1,5-cyclooctadiene (COD) ligand and an anionic Ir bis-NHC complex.

This latter structure represents an unexpected finding. While major advances have been made on oxide supports like silica, where the nature of anchoring sites and the grafting mechanism are nowadays well-understood thanks to surface organometallic chemistry,[31-32] the chemistry of functionalized surfaces with organic ligands is far more challenging and possibly complex, despite its apparent greater resemblance with molecular chemistry. In particular, key differences may occur between the chemistry in solution and in the solid state, where the conformation, the distribution and proximity of the organic/organometallic groups within the materials as well as their interactions with the oxide framework can drastically modify the chemical structure and reactivity of the surface sites, yielding

structures differing from what could be expected in solution. This is illustrated here with the structure of an anionic Ir bis-NHC, revealed here for the first time on a surface and that could not be formed in solution.

Our work not only highlights the great complexity of catalytic materials prepared by surface functionalization, where mixtures of active sites and leftover starting groups may be present, impacting catalytic applications, but also demonstrates the unique capability of DNP SENS DNP SENS in combination with EXAFS and advanced DFT methods to decode this complexity at all stages of the synthesis. The NMR data and the calculation process led to catalytic structures that were initially not postulated nor expected but that could be rationalized experimentally, thus validating the soundness of the structure determination approach.

The rational development of heterogeneous catalysts in the future is expected to proceed through the determination of 3D structures. Our study demonstrates that this goal is now within reach, including on complex, multiple-site catalytic surfaces.

EXPERIMENTAL SECTION

Synthesis of the Materials. Details regarding the synthesis of the six materials are given in the SI, together with elemental analysis and solution NMR data. Catalytic tests are also reported.

NMR Spectroscopy. All DNP SENS experiments were conducted on a Bruker solid-state DNP NMR spectrometer. It consists of a wide-bore 9.4 T magnet ($\omega_{1H}/(2\pi)$ = 400 MHz, $\omega_{29Si}/(2\pi)$ = 79.5 MHz, $\omega_{13C}/(2\pi)$ = 100 MHz, $\omega_{15N}/(2\pi)$ = 40.5 MHz) equipped with an AVANCE III HD console and a triple resonance 3.2 mm low-temperature CPMAS probe. The probe was used in three different configurations, ^{1}H-^{13}C-^{15}N, ^{1}H-^{29}Si-^{15}N, and ^{1}H-^{13}C-^{29}Si with the appropriate insert for each configuration. DNP was achieved by irradiating the sample with microwaves (mw) generated by a fixed frequency gyrotron (263 GHz) and delivered to the probe by a corrugated waveguide.[46] Sapphire rotors were used (with Vespel caps) for optimal microwave penetration and resistance to low temperatures. The cross-effect matching condition was set to the maximum positive enhancement of TEKPOL by sweeping the coil of the spectrometer magnet. The microwave power was optimized to get the highest proton enhancement on the solvent for each sample. The REDOR DNP SENS data were acquired with a spinning frequency of 10 kHz at sample temperature of approximately 110 K. SPINAL64[47] was used for ^{1}H heteronuclear decoupling with 100 kHz ^{1}H nutation frequencies. Experimental details for the ^{13}C-{^{15}N}, ^{29}Si-{^{13}C}, ^{29}Si-{^{15}N} REDOR and for ^{29}Si-{^{13}C} FS-REDOR experiments (number of scans, experimental times, number of points in each curve…) are summarized in Table S2, S3 and S4. For FS-REDOR, selective inversion of the C6 resonance was achieved using a Gaussian cascade Q3 shaped excitation pulse[48] of 0.8 ms. Before structure calculation, the scaling factor of each REDOR curve was determined from REDOR and FS-REDOR data corresponding to internuclear distances that are fixed in the molecular geometry as described in the SI. TEKPOL radical was provided by Prof. Olivier Ouari (Aix-Marseille University) and prepared according to the synthesis reported in reference [40].

Extended X-ray Absorption Fine Structure (EXAFS). XAS measurements were carried out at the Ir L_3-edge at the SuperXAS beamline at SLS (PSI, Villigen, Switzerland). The storage ring was operated at 2.4 GeV in top-up mode with a ring current of around 400 mA. The incident photon beam provided by a 2.9 T super bend magnet source was selected by a Si(111) quick-EXAFS monochromator and the rejection of higher harmonics and focusing were achieved by a rhodium-coated collimating mirror at 2.8 mrad and a rhodium-coated torroidal mirror at 2.8 mrad. The beam size on the sample was 100 x 100 μm. During the measurements the monochromator was rotating with 10 Hz frequency in 2 deg angular range and X-ray absorption spectra were collected in transmission mode using ionization chambers specially developed for quick data collection with 1 MHz frequency.[49]. The spectra were collected for 2 min and averaged. Calibration of the beamline energy was performed using Pt reference foil (Pt L_3-edge position at 11564 eV). To avoid contact with air all samples were filled in quartz capillaries (0.01 mm wall thickness, 0.9 mm outer diameter; Hilgenberg GmbH) in a glovebox and sealed with Apiezon vacuum grease and wax, and stored in glass tubes under argon that were opened just before the measurements. Data were analyzed by standard procedures[50] using Ifeffit program package.[51] The EXAFS data were fitted in R-space (1–2.4 Å) after a Fourier transform (k = 3–12.5 $Å^{-1}$) using a k-weight of 3. $S0^2$ values were obtained by fitting IrO_2 for Ir L_3 edge.

Computation for the Structure Determination Procedure. The overall procedure is detailed in Figure S25. Calculations were performed using MathWorks Matlab software (versions R2016A or R2018B). The processed Topspin NMR data were imported into MatLab with the ReadBruker2D script developed by the National Magnetic Resonance Facility at Madison (NMRFAM) of the University of Wisconsin-Madison, published under the GNU General Public License v3. Deconvolution was performed using the peakfit v2.0 MatLab script available on the MathWorks File Exchange platform under BSD license.

Computational Modeling. Density functional theory (DFT) calculations were performed with the Amsterdam Density Functional (ADF) software suite, version 2019[52-54] using the Graham supercomputer (Compute Ontario/University of Waterloo) within the Compute Canada network. The procedures used in the present study are highly similar to those reported in the literature.[29] Full details, including modifications to the prior protocol, can be found in the Supporting Information. Realistic amorphous silica surface models were created starting from those published previously by Ugliengo *et al.*[44] For the imidazolium precursor and the Ag-NHC intermediate complex, the appropriate ligand was then placed on the silica surface model in the conformation predicted from the DNP SENS NMR data, along with a TMS moiety but with modifications necessary to accommodate the silica surface and tether the ligand in a sensible place. The most substantial change made was the Si_{T3}-$Si_{Q4'}$ distance, which was not determined precisely during this study. All starting geometries (i.e., prior to any optimization) can be found in the SI.

All geometry optimizations under DFT were carried out at the generalized gradient approximation (GGA) level of theory using the Perdew, Burke, and Ernzerhof (PBE) exchange-correlation functional.[55-56] Dispersion effects were included using the four parameter formulation suggested by Grimme and co-workers,[57] which was invoked using the 'Disperson Grimme3 BJDAMP' string. Effects due to the TCE solvent molecules were treated using the COnductor-like Screening Model (COSMO),[58-60] as implemented in ADF.[61] For geometry optimizations, relativistic effects were included at the scalar level under the zeroth-order regular approximation (ZORA).[62-64] Calculations typically used triple-ζ basis sets (either 'TZP' or 'TZ2P' according to the ADF naming scheme), although in some instances alternative basis sets were used (see Supporting Information for details).

Typically, after placing the ligand and the TMS group on the silica surface, a full geometry optimization of the cluster was performed. Exceptions are outlined in the SI. The optimization calculations used frozen core basis sets (excepting H, which was all-electron). Optimized geometries for species associated with **Mat-NHC-Ir** are depicted in Figure 5, and all structures are provided in the SI (in .mol2 and .xyz formats). Full details regarding all options and processes used for the DFT computations can be found in the SI. Cluster sizes used during the geometry optimizations noted above ranged from 276 to 425 atoms, which were too large to subject to meaningful NMR property calculations with the computational resources available. Further, clusters of this size are rarely relevant as magnetic shielding is a local physical phenomenon. As such, prior to NMR property calculations, all optimized structures were trimmed and terminated with hydrogen atoms where appropriate. Trimmed cluster sizes ranged from 105 to 238 atoms. The atomic positions of the newly-added H atoms were then optimized using a very similar approach as noted earlier. At this point, NMR property calculations were performed on the trimmed and optimized clusters. Further details specific to the NMR property calculations are provided in the SI.

ASSOCIATED CONTENT

Supporting Information

The Supporting Information is available free of charge on the ACS Publications website.
Structure coordinate files (ZIP).
Supplementary experimental details on the synthesis and on the NMR methods, on the material characterization. Additional NMR spectra and Tables of experimental and calculated chemical shifts (PDF).

AUTHOR INFORMATION

Corresponding Author

* anne.lesage@ens-lyon.fr
* chloe.thieuleux@univ-lyon1.fr

ACKNOWLEDGMENT

CMW would like to thank the Vice-President (Research) at the University of Regina and the Faculty of Science at the University of Regina for laboratory startup funds. This research was enabled in part by support provided by Compute Ontario (computeontario.ca) and Compute Canada (www.computecanada.ca). Financial support from ANR-17-CE29-0006-01 is gratefully acknowledged. This work has been supported by the Common Research Laboratory CARMEN (ENS de Lyon, CNRS, IFPEN, Claude Bernard Lyon 1 University, Sorbonne University, and University of Strasbourg). Financial support from the IR INFRANALYTICS FR2054 for conducting the research is gratefully acknowledged. This study is part of a project that has received funding from the European Union's Horizon 2020 research and innovation programme under Grant Agreement No 101008500 ("PANACEA"). Dr G. Pintacuda is greatly acknowledged for constructive discussion on the work.

REFERENCES

1. Serna, P.; Gates, B. C., Molecular Metal Catalysts on Supports: Organometallic Chemistry Meets Surface Science. *Acc. Chem. Res.* **2014,** *47*, 2612-2620.
2. Samantaray, M. K.; Pump, E.; Bendjeriou-Sedjerari, A.; D'Elia, V.; Pelletier, J. D. A.; Guidotti, M.; Psaro, R.; Basset, J.-M., Surface organometallic chemistry in heterogeneous catalysis. *Chem. Soc. Rev.* **2018,** *47*(22), 8403-8437.
3. Copéret, C.; Allouche, F.; Chan, K. W.; Conley, M. P.; Delley, M. F.; Fedorov, A.; Moroz, I. B.; Mougel, V.; Pucino, M.; Searles, K.; Yamamoto, K.; Zhizhko, P. A., Bridging the Gap between Industrial and Well-Defined Supported Catalysts. *Angew. Chim. Int. Ed. Engl.* **2018,** *57*(22), 6398-6440.
4. Hübner, S.; de Vries, J. G.; Farina, V., Why Does Industry Not Use Immobilized Transition Metal Complexes as Catalysts? *Adv. Synth. Catal.* **2015,** *358*(1), 3-25.
5. Copéret, C.; Liao, W.-C.; Gordon, C. P.; Ong, T.-C., Active Sites in Supported Single-Site Catalysts: An NMR Perspective. *J. Am. Chem. Soc.* **2017,** *139*(31), 10588-10596.
6. Weiland, E.; Springuel-Huet, M.-A.; Nossov, A.; Gédéon, A., 129Xenon NMR: Review of recent insights into porous materials. *Micropor. Mesopor. Mat.* **2016,** *225*(c), 41-65.
7. Estes, D. P.; Siddiqi, G.; Allouche, F.; Kovtunov, K. V.; Safonova, O. V.; Trigub, A. L.; Koptyug, I. V.; Coperet, C., C-H Activation on Co,O Sites: Isolated Surface Sites versus Molecular Analogs. *J. Am. Chem. Soc.* **2016,** *138*(45), 14987-14997.
8. Burueva, D. B.; Kovtunova, L. M.; Bukhtiyarov, V. I.; Kovtunov, K. V.; Koptyug, I. V., Single-Site Heterogeneous Catalysts: From Synthesis to NMR Signal Enhancement. *Chem. Eur. J.* **2018,** *25*(6), 1420-1431.
9. Rossini, A. J.; Zagdoun, A.; Lelli, M.; Lesage, A.; Copéret, C.; Emsley, L., Dynamic Nuclear Polarization Surface Enhanced NMR Spectroscopy. *Acc. Chem. Res.* **2013,** *46*(9), 1942-1951.
10. Kobayashi, T.; Perras, F. A.; Slowing, I. I.; Sadow, A. D.; Pruski, M., Dynamic Nuclear Polarization Solid-State NMR in Heterogeneous Catalysis Research. *ACS Catal.* **2015,** *5*, 7055-7062.
11. Berruyer, P.; Emsley, L.; Lesage, A., "DNP in Materials Science: Touching the Surface" in: Encyclopedia of Magnetic Resonance Online. *eMagRes* **2018,** *7*, 93-104.
12. Hooper, R. W.; Klein, B. A.; Michaelis, V. K., Dynamic Nuclear Polarization (DNP) 101: A New Era for Materials. *Chem. Mater.* **2020,** *32*, 4425-4430.
13. Perras, F. A.; Wang, Z.; Naik, P.; Slowing, I. I.; Pruski, M., Natural Abundance 17O DNP NMR Provides Precise O—H Distances and Insights into the Brønsted Acidity of Heterogeneous Catalysts. *Angew. Chim. Int. Ed. Engl.* **2017,** *56*(31), 9165-9169.
14. Moroz, I. B.; Larmier, K.; Liao, W. C.; Coperet, C., Discerning gamma-Alumina Surface Sites with Nitrogen-15 Dynamic Nuclear Polarization Surface Enhanced NMR Spectroscopy of Adsorbed Pyridine. *J. Phys. Chem. C* **2018,** *122*(20), 10871-10882.
15. Johnson, R. L.; Perras, F. A.; Hanrahan, M. P.; Mellmer, M.; Garrison, T. F.; Kobayashi, T.; Dumesic, J. A.; Pruski, M.; Rossini, A. J.; Shanks, B. H., Condensed Phase Deactivation of Solid Bronsted Acids in the Dehydration of Fructose to Hydroxymethylfurfural. *ACS Catal.* **2019,** *9* (12), 11568-11578.
16. Nagashima, H.; Trebosc, J.; Kon, Y.; Sato, K.; Lafon, O.; Amoureux, J.-P., Observation of Low-γ Quadrupolar Nuclei by Surface-Enhanced NMR Spectroscopy. *J. Am. Chem. Soc.* **2020,** *142*, 10659-10672.
17. Ong, T.-C.; Liao, W.-C.; Mougel, V.; Gajan, D.; Lesage, A.; Emsley, L.; Copéret, C., Atomistic Description of Reaction Intermediates for Supported Metathesis Catalysts Enabled by DNP SENS. *Angew. Chim. Int. Ed. Engl.* **2016,** *55*(15), 4743-4747.
18. Xiao, D.; Xu, S.; Brownbill, N. J.; Paul, S.; Chen, L.-H.; Pawsey, S.; Aussenac, F.; Su, B.-L.; Han, X.; Bao, X.; Liu, Z.; Blanc, F., Fast detection and structural identification of carbocations on zeolites by dynamic nuclear polarization enhanced solid-state NMR. *Chem. Sci.* **2018,** *9* (43), 8184-8193.
19. Samantaray, M. K.; Alauzun, J.; Gajan, D.; Kavitake, S.; Mehdi, A.; Veyre, L.; Lelli, M.; Lesage, A.; Emsley, L.; Copéret, C.; Thieuleux, C., Evidence for Metal–Surface Interactions and Their Role in Stabilizing Well-Defined Immobilized Ru–NHC Alkene Metathesis Catalysts. *J. Am. Chem. Soc.* **2013,** *135*(8), 3193-3199.
20. Perras, F. A.; Padmos, J. D.; Johnson, R. L.; Wang, L.-L.; Schwartz, T. J.; Kobayashi, T.; Horton, J. H.; Dumesic, J. A.; Shanks, B. H.; Johnson, D. D.; Pruski, M., Characterizing Substrate–Surface Interactions on Alumina-Supported Metal Catalysts by Dynamic Nuclear Polarization-Enhanced Double-Resonance NMR Spectroscopy. *J. Am. Chem. Soc.* **2017,** *139*(7), 2702-2709.

21. Conley, M. P.; Drost, R. M.; Baffert, M.; Gajan, D.; Elsevier, C.; Oschkinat, H.; Veyre, L.; Zagdoun, A.; Rossini, A.; Lelli, M.; Lesage, A.; Casano, G.; Ouari, O.; Tordo, P.; Emsley, L.; Copéret, C.; Thieuleux, C., A Well-Defined Pd Hybrid Material for the Z-Selective Semihydrogenation of Alkynes Characterized at the Molecular Level by DNP SENS. *Chem. Eur. J.* **2013,** *19* (37), 12234-12238.
22. Gutmann, T.; Liu, J. Q.; Rothermel, N.; Xu, Y. P.; Jaumann, E.; Werner, M.; Breitzke, H.; Sigurdsson, S. T.; Buntkowsky, G., Natural Abundance N-15 NMR by Dynamic Nuclear Polarization: Fast Analysis of Binding Sites of a Novel Amine-Carboxyl-Linked Immobilized Dirhodium Catalyst. *Chem. Eur. J.* **2015,** *21* (9), 3798-3805.
23. Pump, E.; Viger-Gravel, J.; Abou-Hamad, E.; Samantaray, M. K.; Hamzaoui, B.; Gurinov, A.; Anjum, D. H.; Gajan, D.; Lesage, A.; Bendjeriou-Sedjerari, A.; Emsley, L.; Basset, J.-M., Reactive surface organometallic complexes observed using dynamic nuclear polarization surface enhanced NMR spectroscopy. *Chem. Sci.* **2017,** *8*, 284-290.
24. Liao, W. C.; Ong, T. C.; Gajan, D.; Bernada, F.; Sauvee, C.; Yulikov, M.; Pucino, M.; Schowner, R.; Schwarzwalder, M.; Buchmeiser, M. R.; Jeschke, G.; Tordo, P.; Ouari, O.; Lesage, A.; Emsley, L.; Coperet, C., Dendritic polarizing agents for DNP SENS. *Chem. Sci.* **2017,** *8* (1), 416-422.
25. Liu, J. Q.; Groszewicz, P. B.; Wen, Q. B.; Thankamony, A. S. L.; Zhang, B.; Kunz, U.; Sauer, G.; Xu, Y. P.; Gutmann, T.; Buntkowsky, G., Revealing Structure Reactivity Relationships in Heterogenized Dirhodium Catalysts by Solid-State NMR Techniques. *J. Phys. Chem. C* **2017,** *121* (32), 17409-17416.
26. Aljuhani, M. A.; Barman, S.; Abou-Hamad, E.; Gurinov, A.; Ould-Chikh, S.; Guan, E.; Jedidi, A.; Cavallo, L.; Gates, B. C.; Pelletier, J. D. A.; Basset, J. M., Imine Metathesis Catalyzed by a Silica-Supported Hafnium Imido Complex. *ACS Catal.* **2018,** *8* (10), 9440-9446.
27. Pump, E.; Bendjeriou-Sedjerari, A.; Viger-Gravel, J.; Gajan, D.; Scotto, B.; Samantaray, M. K.; Abou-Hamad, E.; Gurinov, A.; Almaksoud, W.; Cao, Z.; Lesage, A.; Cavallo, L.; Emsley, L.; Basset, J. M., Predicting the DNP-SENS efficiency in reactive heterogeneous catalysts from hydrophilicity. *Chem. Sci.* **2018,** *9* (21), 4866-4872.
28. Aljuhani, M. A.; Zhang, Z. Y.; Barman, S.; El Eter, M.; Failvene, L.; Ould-Chikh, S.; Guan, E. J.; Abou-Hamad, E.; Emwas, A. H.; Pelletier, J. D. A.; Gates, B. C.; Cavallo, L.; Basset, J. M., Mechanistic Study of Hydroamination of Alkyne through Tantalum-Based Silica-Supported Surface Species. *ACS Catal.* **2019,** *9* (9), 8719-8725.
29. Berruyer, P.; Lelli, M.; Conley, M. P.; Silverio, D. L.; Widdifield, C. M.; Siddiqi, G.; Gajan, D.; Lesage, A.; Copéret, C.; Emsley, L., Three-Dimensional Structure Determination of Surface Sites. *J. Am. Chem. Soc.* **2017,** *139* (2), 849-855.
30. Perras, F. A.; Paterson, A. L.; Syed, Z. H.; Kropf, A. J.; Kaphan, D. M.; Delferro, M.; Pruski, M., Revealing the Configuration and Conformation of Surface Organometallic Catalysts with DNP-Enhanced NMR. *J. Phys. Chem. C* **2021,** *125* (24), 13433-13442.
31. Coperet, C.; Comas-Vives, A.; Conley, M. P.; Estes, D. P.; Fedorov, A.; Mougel, V.; Nagae, H.; Nunez-Zarur, F.; Zhizhko, P. A., Surface Organometallic and Coordination Chemistry toward Single-Site Heterogeneous Catalysts: Strategies, Methods, Structures, and Activities. *Chem. Rev.* **2016,** *116* (2), 323-421.
32. Samantaray, M. K.; D'Eia, V.; Pump, E.; Falivene, L.; Harb, M.; Chikh, S. O.; Cavallo, L.; Basset, J. M., The Comparison between Single Atom Catalysis and Surface Organometallic Catalysis. *Chem. Rev.* **2020,** *120* (2), 734-813.
33. Romanenko, I.; Gajan, D.; Sayah, R.; Crozet, D.; Jeanneau, E.; Lucas, C.; Leroux, L.; Veyre, L.; Lesage, A.; Emsley, L.; Lacote, E.; Thieuleux, C., Iridium(I)/N-Heterocyclic Carbene Hybrid Materials: Surface Stabilization of Low-Valent Iridium Species for High Catalytic Hydrogenation Performance. *Angew. Chim. Int. Ed. Engl.* **2015,** *54* (44), 12937-12941.
34. Romanenko, I.; Jaffeux, L.; Veyre, L.; Lacote, E.; Meille, V.; Thieuleux, C., A Solid Iridium Catalyst for Diastereoselective Hydrogenation. *Chem. Eur. J.* **2017,** *23* (64), 16171-16173.
35. Maishal, T. K.; Alauzun, J.; Basset, J.-M.; Copéret, C.; Corriu, R. J. P.; Jeanneau, E.; Mehdi, A.; Reyé, C.; Veyre, L.; Thieuleux, C., A Tailored Organometallic-Inorganic Hybrid Mesostructured Material: A Route to a Well-Defined, Active, and Reusable Heterogeneous Iridium-NHC Catalyst for H/D Exchange. *Angew. Chim. Int. Ed. Engl.* **2008,** *47* (45), 8654-8656.
36. Gajan, D.; Schwarzwalder, M.; Conley, M. P.; Gruning, W. R.; Rossini, A. J.; Zagdoun, A.; Lelli, M.; Yulikov, M.; Jeschke, G.; Sauvee, C.; Ouari, O.; Tordo, P.; Veyre, L.; Lesage, A.; Thieuleux, C.; Emsley, L.; Coperet, C., Solid-Phase Polarization Matrixes for Dynamic Nuclear Polarization from Homogeneously Distributed Radicals in Mesostructured Hybrid Silica Materials. *J. Am. Chem. Soc.* **2013,** *135* (41), 15459-15466.
37. Kobayashi, T.; Pruski, M., Spatial Distribution of Silica-Bound Catalytic Organic Functional Groups Can Now Be Revealed by Conventional and DNP-Enhanced Solid-State NMR Methods. *ACS Catal.* **2019,** *9* (8), 7238-7249.
38. Kobayashi, T.; Singappuli-Arachchige, D.; Wang, Z. R.; Slowing, II; Pruski, M., Spatial distribution of organic functional groups supported on mesoporous silica nanoparticles: a study by conventional and DNP-enhanced Si-29 solid-state NMR. *Phys. Chem. Chem. Phys.* **2017,** *19* (3), 1781-1789.
39. Zagdoun, A.; Rossini, A. J.; Conley, M. P.; Grüning, W. R.; Schwarzwälder, M.; Lelli, M.; Franks, W. T.; Oschkinat, H.; Copéret, C.; Emsley, L.; Lesage, A., Improved Dynamic Nuclear Polarization Surface-Enhanced NMR Spectroscopy through Controlled Incorporation of Deuterated Functional Groups. *Angew. Chim. Int. Ed. Engl.* **2013,** *52* (4), 1222-1225.
40. Zagdoun, A.; Casano, G.; Ouari, O.; Schwaerzwalder, M.; Rossini, A. J.; Aussenac, F.; Yulikov, M.; Jeschke, G.; Copéret, C.; Lesage, A.; Tordo, P.; Emsley, L., Large Molecular Weight Nitroxide Biradicals Providing Efficient Dynamic Nuclear Polarization at Temperatures up to 200 K. *J. Am. Chem. Soc.* **2013,** *135*, 12790-12797.
41. Pinon, A. C.; Schlagnitweit, J.; Berruyer, P.; Rossini, A. J.; Lelli, M.; Socie, E.; Tang, M.; Pham, T.; Lesage, A.; Schantz, S.; Emsley, L., Measuring Nano- to Microstructures from Relayed Dynamic Nuclear Polarization NMR. *J. Phys. Chem. C* **2017,** *121* (29), 15993-16005.
42. Gullion, T., Introduction to Rotational-Echo, Double-Resonance NMR. *Concepts Magn. Reson.* **1998,** *10(5)*, 277-289.
43. Jaroniec, C. P.; Tounge, B. A.; Herzfeld, J.; Griffin, R. G., Frequency Selective Heteronuclear Dipolar Recoupling in Rotating Solids: Accurate 13C− 15N Distance Measurements in Uniformly 13C, 15N-labeled Peptides. *J. Am. Chem. Soc.* **2001,** *123* (15), 3507-3519.
44. Ugliengo, P.; Sodupe, M.; Musso, F.; Bush, I. J.; Orlando, R.; Dovesi, R., Realistic Models of Hydroxylated Amorphous Silica Surfaces and MCM-41 Mesoporous Material Simulated by Large-scale Periodic B3LYP Calculations. *eMagRes* **2008,** *20* (23), 4579-4583.
45. Puerta-Oteo, R.; Jimenez, M. V.; Lahoz, F. J.; Modrego, F. J.; Passarelli, V.; Perez-Torrente, J. J., Zwitterionic Rhodium and Iridium Complexes Based on a Carboxylate Bridge-Functionalized Bis-N-heterocyclic Carbene Ligand: Synthesis, Structure, Dynamic Behavior, and Reactivity. *Inorg. Chem.* **2018,** *57* (9), 5526-5543.
46. Rosay, M.; Blank, M.; Engelke, F., Instrumentation for solid-state dynamic nuclear polarization with magic angle spinning NMR. *J. Magn. Reson.* **2016,** *264* (C), 88-98.
47. Fung, B. M.; Khitrin, A. K.; Ermolaev, K., An Improved Broadband Decoupling Sequence for Liquid Crystals and Solids. *J. Magn. Reson.* **2000,** *142*, 97-101.
48. Emsley, L.; bodenhausen, G., Optimization of Shaped Selective Pulses for NMR Using a Quaternion Description of Their Overall Propagators. *J. Magn. Reson.* **1992,** *97*, 135-148.
49. Müller, O.; Stötzel, J.; Lützenkirchen-Hecht, D.; Frahm, R., Gridded Ionization Chambers for Time Resolved X-Ray Absorption Spectroscopy. *J. Phys. Conf. Ser.* **2013,** *425* (9), 092010.
50. Koningsberger, D. C., *X-Ray Absorption, Principles, Applications, Techniques of EXAFS, SECAFS and CANES*. John Wiley and Sons Ltd: New York, Chichester, Brisbane, Toronto, Singapore, 1998.
51. Newville, M., IFEFFIT: interactive XAFS analysis and FEFF fitting. *J. Synchrotron Radiat.* **2001,** *8*, 322-324.
52. Guerra, C. F.; Snijders, J. G.; te Velde, G.; Baerends, E. J., Towards an order-N DFT method. *Theor. Chem. Acc.* **1998,** *99* (6), 391-403.

53. te Velde, G.; Bickelhaupt, F. M.; Baerends, E. J.; Guerra, C. F.; Van Gisbergen, S. J. A.; Snijders, J. G.; Ziegler, T., Chemistry with ADF. *J. Comput. Chem.* **2001,** *22* (9), 931-967.
54. Baerends, E. J.; Ziegler, T.; Atkins, A. J.; Autschbach, J.; Bashford, D.; Baseggio, O.; Bérces, A.; Bickelhaupt, F. M.; Bo, C.; Boerritger, P. M., ADF 2019.3, SCM, Theoretical Chemistry; Vrije Universiteit: Amsterdam, The Netherlands, 2019; Available online: https://www.scm.com (accessed on July 1 2021. **1991**.
55. Perdew, J. P.; Burke, K.; Ernzerhof, M., Generalized gradient approximation made simple. *Phys. Rev. Lett.* **1996,** *77* (18), 3865-3868.
56. Perdew, J. P.; Burke, K.; Ernzerhof, M., Generalized gradient approximation made simple (vol 77, pg 3865, 1996). *Phys. Rev. Lett.* **1997,** *78* (7), 1396-1396.
57. Grimme, S.; Ehrlich, S.; Goerigk, L., Effect of the Damping Function in Dispersion Corrected Density Functional Theory. *J. Comput. Chem.* **2011,** *32* (7), 1456-1465.
58. Klamt, A., Conductor-like screening model for real solvents - a new approach to the quantitative calculation of solvation phenomena. *J. Phys. Chem.* **1995,** *99* (7), 2224-2235.
59. Klamt, A.; Jonas, V., Treatment of the outlying charge in continuum solvation models. *J. Phys. Chem.* **1996,** *105* (22), 9972-9981.
60. Klamt, A.; Schuurmann, G., Cosmo - A new apporach to dielectric screening in solvents with explicit expressions for the screening energy and its gradient. *J. Chem. Soc., Perkin trans. 2* **1993,** (5), 799-805.
61. Pye, C. C.; Ziegler, T., An implementation of the conductor-like screening model of solvation within the Amsterdam density functional package. *Theor. Chem. Acc.* **1999,** *101* (6), 396-408.
62. Van Lenthe, E.; Ehlers, A.; Baerends, E. J., Geometry optimizations in the zero order regular approximation for relativistic effects. *J. Chem. Phys.* **1999,** *110* (18), 8943-8953.
63. Van Lenthe, E.; Baerends, E. J.; Snijders, J. G., Relativistic regular 2-component hamiltonians. *J. Chem. Phys.* **1993,** *99* (6), 4597-4610.
64. Van Lenthe, E.; Baerends, E. J.; Snijders, J. G., Relativistic total-energy using regular apporximations. *J. Chem. Phys.* **1994,** *101* (11), 9783-9792.

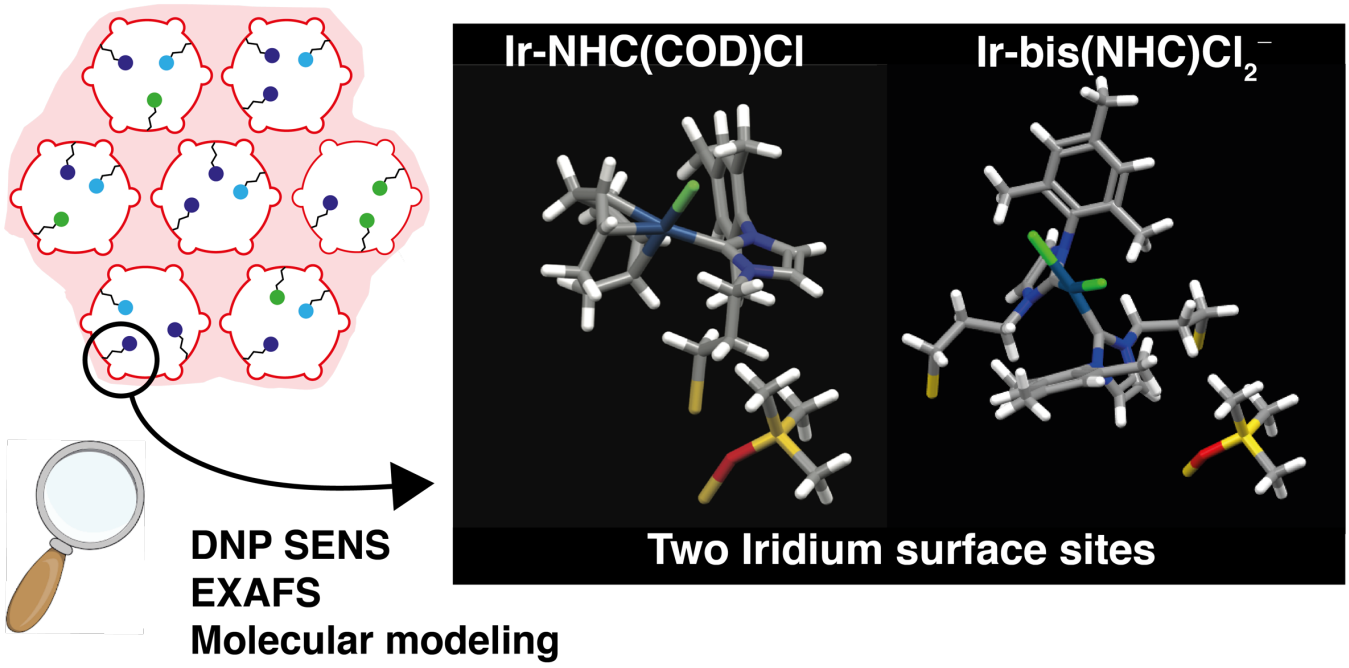

DNP Surface Enhanced NMR Spectroscopy jointly with EXAFS and molecular modeling allows the site-selective structure description with atomic-level resolution of catalytically active iridium supported complexes in a multi-species environment.